

# Electrical and thermal transport in twisted TMDC/CrI<sub>3</sub>-superconducting TMDC junctions

Leyla Majidi<sup>1,\*</sup> and Reza Asgari<sup>2,3,†</sup>

<sup>1</sup>*School of Nano Science, Institute for Research in Fundamental Sciences (IPM), Tehran 19395-5531, Iran*

<sup>2</sup>*School of Physics, Institute for Research in Fundamental Sciences (IPM), Tehran 19395-5531, Iran*

<sup>3</sup>*School of Physics, University of New South Wales, Kensington, NSW 2052, Australia*

(Dated: January 24, 2022)

Wide tunability of the proximity exchange effect between transition metal dichalcogenides (TMDCs) and Chromium trichloride (CrI<sub>3</sub>) heterostructures provides fascinating opportunity for using TMDCs in two-dimensional magnetoelectrics. In this paper, the effect of the twist angle between the monolayer CrI<sub>3</sub> and the TMDC layer as well as the gate electric field on the electrical and thermal transport through a TMDC/CrI<sub>3</sub>-superconducting TMDC junction are investigated by making use of Dirac-Bogoliubov-de Gennes equation. We show substantial quantities can be controlled by spin-splitting of band structures owing to the spin-orbit interaction, and exchange splitting of the bands originates from the proximity effect. The property of Andreev reflection process strongly depends on the spin-valley polarized states owing to the spin-orbit coupling. Perfect Andreev reflection is possible over a large bias voltage range by using a gate voltage to tune the local Fermi energy and varying the type of charge doping. It is detected that the proposed structure with p-type doping has greater spin-valley polarized Andreev conductance and the high thermal conductance. We further demonstrate that twisting can lead to the suppression or enhancement of the Andreev conductance depending on the chemical potential of the TMDC/CrI<sub>3</sub> layer as well as the amplification of the thermal conductance for the chemical potentials less than that of the superconducting region.

## I. INTRODUCTION

Heterostructures composed of superconductors and non-superconducting materials exhibit technologically relevant quantum phenomenon [1–8] including superconducting qubits [9–13], and provide the basis for experimental methods like point-contact spectroscopy [14–16] and scanning tunneling spectroscopy [17, 18]; enabling the determination of the superconducting gap and investigation of the phase diagram in unconventional superconductors [19, 20]. The simplest superconducting heterostructure is a normal metal-superconductor junction. Transmission of the low-energy electrons through this junction is dominated by a particular and intriguing type of fundamental reflection process, Andreev reflection (AR) [21], in which the quasiparticle identity is changed. Besides the normal electron-to-electron reflection, an incident electron upon hitting the normal metal-superconductor interface is retro Andreev reflected as a hole, and a Cooper pair is transmitted to the superconductor. Since the Cooper pair carries a charge of  $2e$  and zero heat, the peculiar AR process results in an enhancement of the electrical conductance and suppression of the thermal conductance [22–24]. The spin dependence of the AR process causes drastic changes in the transport properties, when a ferromagnetic layer is interfaced to a superconductor. A momentum shift of order  $2\hbar/v_F$  between the Andreev reflected electron-hole in the presence of the exchange field,  $h$ , in the ferromagnet reduces

the AR amplitude, and consequently, the conductance reduces from its value for normal metal-superconductor junction and vanishes for a half-metallic ferromagnet [25].

Owing to the interplay of superconductivity and the unique electronic structure of atomically thin two-dimensional (2D) materials, superconducting heterostructures based on 2D materials have received considerable attention in quantum transport, and application of superconducting nanoelectronics [26–39]. Many theoretical and experimental works have found peculiar AR processes at low energies [26–32] and nonlocal processes have been predicted to occur under various conditions [30, 31, 33–37]. In particular, Cooper pair splitting has been observed in graphene [38]. To be specific, interband specular AR has been demonstrated to appear in graphene-based superconducting hybrid structures [26, 30–32] as well as the intraband specular AR in thin films of topological insulators [27, 28], which are absent in ordinary metal-superconductor interfaces. In addition, the ferromagnetic exchange interaction in graphene-based ferromagnetic-superconducting junction can suppress Andreev retro reflection but enhance the specular AR [29].

Van der Waals heterostructures comprising a variety of 2D layered materials have emerged as potential building blocks for the future ultrafast and low-power electronic and spintronic devices [40–42]. The atomically thin nature of 2D materials promotes the design of artificial materials by proximity effects that originate from short-range interactions. Such a designer approach is essential for making materials magnetic without hosting magnetic ions and is particularly compelling for spintronics, which typically harnesses functionalities from thin

\* Leyla.Majidi@ipm.ir

† asgari@ipm.ir

layers of magnetic and non-magnetic materials and the interfaces between them.

For 2D spintronics and the novel field of superconducting spintronics, it is desirable to integrate 2D materials like graphene and transition metal dichalcogenides (TMDCs) with 2D magnets. Semiconducting TMDCs such as  $\text{MX}_2$  ( $\text{M} = \text{W}, \text{Mo}$ ;  $\text{X} = \text{S}, \text{Se}, \text{Te}$ ) possess strong spin-orbit coupling (SOC) as well as the possibility for a coupling of the spin and valley physics, which is owing to the strong spin-orbit coupling and the broken inversion symmetry [43–46]. Recent experiments demonstrate a few meV of proximity exchange in TMDC and  $\text{CrI}_3$  heterostructures. Interestingly, the monolayer of  $\text{CrI}_3$  is a ferromagnet [47–49], while bilayer  $\text{CrI}_3$  shows antiferromagnetic coupling [48, 50, 51]. Unlike thin films of conventional ferromagnets, the 2D layered ferromagnets have magnetization pointing out of the plane, which is a time-reversal breaking analog of the valley Zeeman splitting in TMDCs. For practical applications in electronic devices, the single layer and multilayer TMDCs can be n- or p-type doped on favorable charge carriers [52, 53]. At high carrier concentrations and in the presence of the high- $\kappa$  dielectrics, they undergo a superconducting transition, with a doping-dependent critical temperature [54–57].

Recently, the fascinating research on 2D materials has experienced a modern stage in its development represented by a new degree of freedom in the sense of material structure, a twist angle between the neighboring layers, which facilitates the fine tuning of electronic properties of the van der Waals heterostructures. Stacking 2D van der Waals materials rotated with respect to each other has provided an opportunity to explore a variety of exotic physical phenomena, providing an exciting platform for “twistronics”. The most prominent example is magic-angle twisted bilayer graphene, exhibiting magnetism [58] and superconductivity [59, 60] due to strong correlations. Twistronics is now demonstrating its potential for proximity effects. It is revealed that twisting has profound influences on both the magnitude and the type of proximity induced SOC in graphene/TMDC heterostructure [61] as well as proximity exchange coupling in graphene/ $\text{Cr}_2\text{Ge}_2\text{Te}_6$  heterostructure and emergence of antiferromagnetic Dirac bands in graphene [62]. Remarkably, wide tunability of the proximity exchange coupling has been reported in TMDC/ $\text{CrI}_3$  heterostructures through controlling the interlayer twist between layers and electrostatic gating [63].

Magnetic-superconducting junctions are elementary building blocks for superconducting spintronics, with potential applications in quantum computing. In this paper, we theoretically examine local Andreev reflection through a ferromagnetic (F)/superconducting (S) junction made of proximity exchange-coupled TMDC/ $\text{CrI}_3$  heterostructure as ferromagnet and superconducting TMDC (with  $\text{WSe}_2$  and  $\text{MoSe}_2$  as TMDC). Making use of Dirac-Bogoliubov-de Gennes formalism, we investigate the tunability of AR process and accordingly the

Andreev conductance with respect to the charge doping, twisting the monolayer  $\text{CrI}_3$  relative to the TMDC layer and applying a gate electric field to the magnetized region. For F/S structure with p- or n-type doping, we find that perfect AR can be controlled electrically and visible over a large voltage range; it can be achieved for subgap bias voltages ( $eV < \Delta_S$ ) at the defined chemical potential of the F region,  $\mu_F$ , and for a wide range of  $\mu_F$ , when  $eV = \Delta_S$ . The AR process with spin-valley polarization is equally possible for a defined range of the chemical potential of the F region. We demonstrate that the probability of AR and accordingly the Andreev differential conductance can be suppressed or reduced in the spin-valley polarized AR regime and increased in the non-polarized regime by twisting. The twist angle induced changes in the Andreev conductance strongly depends on the value of the subgap bias voltage: significantly, it increases with the bias voltage at the defined chemical potential of the F region in  $\text{MoSe}_2$ -based structure, while it reduces with the bias voltage and tends to zero for other values of  $\mu_F$  in both  $\text{MoSe}_2$ - and  $\text{WSe}_2$ -based structures, when  $eV = \Delta_S$ . Moreover, the presence of the positive applied electric field in the ferromagnetic region attenuates the Andreev conductance by increasing the proximity exchange coupling.

Next, we investigate the thermal transport characteristics of the proposed structure by evaluating the thermal conductance. The thermal conductance maintains an increasing behavior with the temperature and vanishes at temperatures well below the critical temperature of the superconducting order parameter. We find that twisting can lead to the significant enhancement of the thermal conductance in F/S structures with p-doped F region and reduction of it in the corresponding structure with n-type doping, for the chemical potentials of the F region less than that of the superconducting region. However, gating slightly decreases the thermal conductance of p-doped structures and causes no notable changes in the case of n-doped F/S junctions. Furthermore, we analyze the effect of the type of charge doping on the transport characteristics of the proposed structure and demonstrate the high charge and thermal conductance belongs to the  $\text{WSe}_2$ - and  $\text{MoSe}_2$ -based structures with p-type doping. In the case of F/S junction with diverse types of doping for F and S regions, the enhancement of the charge conductance and AR process with unit efficiency can be restored by increasing the chemical potential of the S region.

Ultimately, we compare the results of the  $\text{WSe}_2$ -based structure with those of the corresponding  $\text{MoSe}_2$ -based structure and observe the amplification of the thermal conductance and attenuation of the Andreev conductance in  $\text{MoSe}_2$ -based structure with p-type doping as well as reduction of the thermal conductance in n-doped structure. In addition, we present substantial changes in the charge and especially thermal conductance of the magnetized gapped graphene/superconducting TMDC and gapped graphene-based structures.

The rest of the paper is arranged as follows. Section

II is devoted to the theoretical model and fundamental formalisms which will be implemented to investigate AR in a twisted TMDC/CrI<sub>3</sub>-superconducting TMDC junction. In Sec. III, we present our numerical results for the Andreev differential conductance and the thermal conductance of the proposed structures. Finally, a brief summary of results is given in Sec. IV.

## II. THEORETICAL FORMALISM

We consider a wide ballistic F/S junction normal to the  $x$  axis with proximity exchange-coupled TMDC/CrI<sub>3</sub> heterostructure (as F region) for  $x < 0$  and superconducting TMDC (as S region) extending over the  $x > 0$  region (with MoSe<sub>2</sub> and WSe<sub>2</sub> as TMDC). The magnetic insulator substrate CrI<sub>3</sub> is weakly coupled to the TMDC by van der Waals forces; preserving the characteristic electronic band structure of the TMDC. The proximity exchange coupling splits the conduction and valence bands of the TMDC by roughly 1-5 meV, and combined with the intrinsic (valley Zeeman) spin-orbit coupling (SOC) of the TMDC lifts the valley degeneracy [63]. The effective low-energy Hamiltonian which describes the proximity effects in TMDC due to CrI<sub>3</sub>, has the form [63]

$$\mathcal{H} = \mathcal{H}_0 + \mathcal{H}_\Delta + \mathcal{H}_{soc} + \mathcal{H}_{ex} + \mathcal{H}_R, \quad (1)$$

$$\mathcal{H}_0 = \hbar v_F s_0 \otimes (\tau \sigma_x k_x + \sigma_y k_y), \quad (2)$$

$$\mathcal{H}_\Delta = \frac{\Delta}{2} s_0 \otimes \sigma_z, \quad (3)$$

$$\mathcal{H}_{soc} = \tau s_z \otimes (\lambda_c \sigma_+ + \lambda_v \sigma_-), \quad (4)$$

$$\mathcal{H}_{ex} = -s_z \otimes (B_c \sigma_+ + B_v \sigma_-), \quad (5)$$

$$\mathcal{H}_R = \lambda_R (\tau s_y \otimes \sigma_x - s_x \otimes \sigma_y). \quad (6)$$

Here,  $\tau = \pm 1$  is the valley index for K (K') point and  $v_F$  represents the Fermi velocity. The pseudospin Pauli matrices  $\sigma_i$  ( $i = 0, x, y, z$ ) act on the conduction and valence band subspaces and  $s_i$  ( $i = 0, x, y, z$ ) refers to real spin. The parameter  $\Delta$  denotes the orbital gap of the spectrum. The spin-splitting of the conduction and valence bands due to the intrinsic SOC is determined by the parameters  $\lambda_c$  and  $\lambda_v$ , respectively. Proximity exchange effects are presented with  $B_c$  and  $B_v$  describing the proximity-induced exchange splitting of the conduction and valence bands. The Rashba SOC parameter  $\lambda_R$  is due to the presence of the inversion asymmetry in the heterostructure. For the seek of simplicity, we introduce  $\sigma_\pm = (\sigma_0 \pm \sigma_z)/2$ .

Recently, wide tunability of the proximity exchange in monolayer MoSe<sub>2</sub> and WSe<sub>2</sub> owing to a ferromagnetic monolayer CrI<sub>3</sub> has been explored with respect to twisting and gating [63]. In particular, proximity exchange splittings depend on the twist angle between the TMDC and the CrI<sub>3</sub>. Not only do the magnitudes of the exchange differ, but also, remarkably, the direction of the exchange field for the valence band changes sign. Moreover, the proximity exchange parameters increase when the electric field is turned from negative to positive

values, which enables the gate control of proximity exchange. We should mention the gap parameter, as well as the Fermi velocity, are not affected by external electric fields.

The S part can be produced by depositing a superconducting electrode on the top of the TMDC sheet. In this region, exchange parameters are zero and the superconducting correlations are characterized by the superconducting pair potential (order parameter)  $\Delta_S$ , which is taken to remain a constant.

Transport takes place in the  $x$  direction, and we assume perfectly flat and clean interfaces. Transport in such junction is described by Dirac-Bogoliubov-de Gennes (DBdG) equation [26, 64]

$$\begin{pmatrix} \mathcal{H} + U(\mathbf{r}) - \mu_0 & \tilde{\Delta}_S \\ \tilde{\Delta}_S^\dagger & \mu_0 - [\mathcal{T}\mathcal{H}\mathcal{T}^{-1} + U(\mathbf{r})] \end{pmatrix} \begin{pmatrix} u \\ v \end{pmatrix} = \varepsilon \begin{pmatrix} u \\ v \end{pmatrix}, \quad (7)$$

where  $\varepsilon$  is the excitation energy,  $\mu_0$  is the chemical potential,  $U(r)$  denotes an electrostatic potential and  $\mathcal{T}$  represents the time-reversal operator. Substituting the effective single-particle Hamiltonian  $\mathcal{H}$  [Eq. (1)], time-reversal operator  $\mathcal{T} = i\tau_x s_y \mathcal{K}$  (with  $\mathcal{K}$  the operator of the complex conjugation), and the pair potential  $\tilde{\Delta}_S = s_0 \otimes \sigma_x \Delta_S e^{i\varphi}$  into Eq. (7), results in two decoupled sets of four-dimensional DBdG equations for given spin  $s$  and valley  $\tau$ , which each of them possesses the form [37]

$$\begin{pmatrix} H_{s,\tau}^e - \mu & \Delta_S e^{i\varphi} \\ \Delta_S e^{-i\varphi} & \mu - H_{s,\tau}^h \end{pmatrix} \begin{pmatrix} u_{s,\tau} \\ v_{\bar{s},\bar{\tau}} \end{pmatrix} = \varepsilon \begin{pmatrix} u_{s,\tau} \\ v_{\bar{s},\bar{\tau}} \end{pmatrix}, \quad (8)$$

where  $\mu = \mu_0 - U(r)$  and the electrostatic potential  $U(r)$  is taken to be  $-U_0$  in the S region and  $U(r) = 0$  in the F region. It is reasonable to assume that the chemical and pair potentials  $\mu_0$  and  $\Delta_S$  are constant in each region. The pair potential is zero in the F region, which is a good approximation if the superconducting coherence length is appreciably larger than the Fermi wavelength. The superconducting phase  $\varphi$  only plays a role in junctions with several superconductors, and hence we omit it here. The electron and hole wave functions,  $u_{s,\tau}$  and  $v_{\bar{s},\bar{\tau}}$ , are two-component spinors of the form  $(\psi_c, \psi_v)$ , where  $c$  and  $v$  denote the conduction and valence bands, respectively. Therefore, the electron excitations in one valley are coupled by the superconducting pair potential  $\Delta_S$  to hole excitations in the other valley.

To study Andreev reflection at the F/S interface within the scattering formalism, we first construct the quasi-particle wave functions that participate in the scattering processes. According to Eq. (8), the dynamics of the low-energy itinerant charge carriers inside the F region with spin  $s$  from valley  $\tau$  are described by effective Hamiltonians  $H_{s,\tau}^e$  and  $H_{s,\tau}^h$ , respectively, for the electron and hole subsectors,

$$\begin{aligned} H_{s,\tau}^{e(h)} &= \hbar v_F (\tau \sigma_x k_x + \sigma_y k_y) + \frac{\Delta}{2} \sigma_z + s\tau (\lambda_c \sigma_+ + \lambda_v \sigma_-) \\ &\quad - s(\bar{s})(B_c \sigma_+ + B_v \sigma_-). \end{aligned} \quad (9)$$

The Rashba parameter  $\lambda_R$  is set to zero, since there is no in-plane component of the spin expectation value around the band edges, and therefore, it is unnecessary to capture the essentials of the band structure for the TMDC/CrI<sub>3</sub> stacks. At a given energy  $\varepsilon$  and a transverse momentum  $k_y$ , the solutions are two states of the form

$$\psi_c^{e\pm} = A_{s,\tau}^e e^{\pm i\tau k_x^e x} e^{ik_y y} \begin{pmatrix} \pm \tau a_{s,\tau}^e e^{\mp i\tau \theta_{s,\tau}^e} \\ 1 \\ 0 \\ 0 \end{pmatrix}, \quad (10)$$

for the conduction band electrons with energy-momentum relation

$$\varepsilon_c^e = -\mu_F + \frac{1}{2}[-s(B_c + B_v) + s\tau(\lambda_c + \lambda_v)] + \sqrt{4(\hbar v_F |\mathbf{k}_{s,\tau}^e|)^2 + ([s(B_c + B_v) + \Delta] + s\tau(\lambda_c - \lambda_v))^2} \quad (11)$$

and

$$\psi_c^{h\pm} = A_{s,\tau}^h e^{\mp i\tau k_x^h x} e^{ik_y y} \begin{pmatrix} 0 \\ 0 \\ \mp \tau a_{s,\tau}^h e^{\pm i\tau \theta_{s,\tau}^h} \\ 1 \end{pmatrix}, \quad (12)$$

for the conduction band holes of n-doped TMDC with energy-momentum relation

$$\varepsilon_c^h = \mu_F - \frac{1}{2}[-\bar{s}(B_c + B_v) + s\tau(\lambda_c + \lambda_v)] + \sqrt{4(\hbar v_F |\mathbf{k}_{s,\tau}^h|)^2 + ([\bar{s}(B_c + B_v) + \Delta] + s\tau(\lambda_c - \lambda_v))^2}. \quad (13)$$

As seen here, the spin-splitting and exchange splitting of the conduction and valence bands appear in the eigenvalues and eigenvectors and subsequently the transport properties varies with changing those quantities. In Eqs. (10) and (12),  $\mu_F = \mu_0$ ,  $a_{s,\tau}^{e(h)} = [\mu_F + (-)\varepsilon + s(\bar{s})B_v - s\tau\lambda_v + \Delta/2]/\hbar v_F |\mathbf{k}_{s,\tau}^{e(h)}|$ ,  $A_{s,\tau}^{e(h)} = 1/\sqrt{2 a_{s,\tau}^{e(h)} \cos(\tau\theta_{s,\tau}^{e(h)})}$ , and  $\theta_{s,\tau}^{e(h)} = \arcsin(k_y/|\mathbf{k}_{s,\tau}^{e(h)}|)$  is the angle of the propagation of the electron (hole). The two propagation directions of the electron (hole) along the  $x$ -axis are denoted by  $\pm$  in  $\psi_c^{e(h)\pm}$ .

In pristine TMDC monolayers, the two valleys are the same due to the time-reversal symmetry. The vicinity to the 2D magnetic material CrI<sub>3</sub> provides a direct and effective way to break the valley degeneracy of TMDC because of the magnetic proximity effect. The presence of negative proximity exchange field in TMDC/CrI<sub>3</sub> heterostructure [63] shifts the spin- $s$  subband of the  $\tau$  ( $\bar{\tau}$ ) valley upward and the spin- $\bar{s}$  subband of the  $\tau$  ( $\bar{\tau}$ ) valley downward in the conduction and valence bands, respectively, by  $|B_c|$  and  $|B_v|$ . In contrast, twisting the CrI<sub>3</sub> layer with respect to the monolayer TMDC replaces the sign of the proximity exchange in the valence band

(see Table. I) and therefore brings the spin-subbands of the  $\tau$ -valley close to each other and gets those of the  $\bar{\tau}$  valley far away from each other. Therefore, the proximity exchange coupling adjusts the valley splitting and the TMDC/CrI<sub>3</sub> heterostructure shows valley polarization of the TMDC [37, 65].

Inside the S region, the solutions are rather mixed electron-hole excitations (called Dirac-Bogoliubov quasiparticles) that either decay exponentially as  $x \rightarrow \infty$  (for subgap solutions when  $\varepsilon \leq \Delta_S$ ) or propagate along the  $x$  direction (for supragap solutions when  $\varepsilon > \Delta_S$ ). These solutions for the n-doped S region take the form

$$\psi_c^{S\pm} = e^{i\tau k'_{\pm,x} x} e^{ik_y y} \begin{pmatrix} u_{1\pm} \\ u_2 \\ u_{3\pm} \\ 1 \end{pmatrix}, \quad (14)$$

where

$$u_{1\pm} = \frac{1}{4\hbar v_F \Delta_S (\tau k'_{\pm,x} + ik_y)} [4(\hbar v_F k_{S\pm})^2 + \Delta^2 - \frac{1}{2\mu_S - s\tau(\lambda_c + \lambda_v)} [s\tau(\lambda_c - \lambda_v)[-2\mu_S + s\tau(\lambda_c + \lambda_v) - B](-2\mu_S + 2s\tau\lambda_c + 2\varepsilon) + \Delta(-2\mu_S + s\tau(3\lambda_c - \lambda_v) + \frac{B}{2\mu_S - s\tau(\lambda_c + \lambda_v)} + 2\varepsilon)], \quad (15)$$

$$u_2 = \frac{1}{4\mu_S \Delta_S - 2s\tau \Delta_S (\lambda_c + \lambda_v)} (B + [2\mu_S - s\tau(\lambda_c + \lambda_v)] \times [-2\mu_S + s\tau(\lambda_c + \lambda_v) + 2\varepsilon]), \quad (16)$$

$$u_{3\pm} = -\frac{1}{2\hbar v_F (\tau k'_{\pm,x} + ik_y) [-2\mu_S + s\tau(\lambda_c + \lambda_v)]} ([\Delta + s\tau(\lambda_c - \lambda_v)][2\mu_S - s\tau(\lambda_c + \lambda_v)] + B), \quad (17)$$

$\mu_S = \mu_0 + U_0$ ,  $k'_{\pm,x} = \pm k_0 + ik\tau$ ,  $k_{S\pm} = (2\hbar v_F)^{-1} [4(\mu_S^2 + \varepsilon^2 - \Delta_S^2 - s\tau\mu_S(\lambda_c + \lambda_v) + \lambda_c\lambda_v \pm \sqrt{(\varepsilon^2 - \Delta_S^2)[2\mu_S - s\tau(\lambda_c + \lambda_v)]^2} + 2s\tau\Delta(\lambda_v - \lambda_c) - \Delta^2)$ , and  $B = ([-2\mu_S + s\tau(\lambda_c + \lambda_v)]^2 [4(\hbar v_F k_{S\pm})^2 + \Delta^2 + 2s\tau\Delta(\lambda_c - \lambda_v) + (\lambda_c - \lambda_v)^2])^{1/2}$ .

An incident electron from the conduction band of n-doped F regions with a subgap energy  $0 \leq \varepsilon \leq \Delta_S$  could undergo two possible scattering events. It can either be normally reflected as an electron in the conduction band via normal reflection (NR), or be Andreev reflected as a hole in the same band with opposite spin and different valley index via retro AR. Denoting the amplitudes of the NR, and AR processes  $r_{e,s,\tau}^{s,\tau}$  and  $r_{h,\bar{s},\bar{\tau}}^{s,\bar{\tau}}$ , respectively, the total wave functions inside the F and S regions can be written as

$$\psi_F = \psi_c^{e+} + r_{s,\tau}^e \psi_c^{e-} + r_{\bar{s},\bar{\tau}}^h \psi_c^{h-}, \quad (18)$$

$$\psi_S = t \psi_c^{S+} + t' \psi_c^{S-}. \quad (19)$$

Matching the wave functions of the F and S regions at the interface  $x = 0$ , the scattering coefficients for the normal and Andreev reflection processes can be obtained. Having known the reflection coefficients, we investigate the charge and thermal conductance of the F/S interface in the following section.



<i>Structure</i>	$\Delta$ (eV)	$\lambda_c$ (meV)	$\lambda_v$ (meV)	$B_c$ (meV)	$B_v$ (meV)
Bare WSe <sub>2</sub>	1.327	13.90	241.79	0	0
WSe <sub>2</sub> /CrI <sub>3</sub> (no SOC, no twist)	1.358	-	-	-2.223	-1.446
WSe <sub>2</sub> /CrI <sub>3</sub> (with SOC, no twist)	1.327	13.81	240.99	-1.783	-1.583
WSe <sub>2</sub> /CrI <sub>3</sub> (no SOC, with twist 30°)	1.417	-	-	-1.648	1.896
Bare MoSe <sub>2</sub>	1.302	-9.647	94.56	-	-
MoSe <sub>2</sub> /CrI <sub>3</sub> (no SOC, no twist)	1.305	-	-	-2.081	-1.454
MoSe <sub>2</sub> /CrI <sub>3</sub> (with SOC, no twist)	1.301	-9.678	94.43	-1.592	-1.426
MoSe <sub>2</sub> /CrI <sub>3</sub> (no SOC, with twist 30°)	1.351	-	-	-1.641	0.502

TABLE I. The orbital gap  $\Delta$ , spin-orbit coupling (SOC)  $\lambda_{c(v)}$  and the proximity exchange  $B_{c(v)}$  of the conduction (valence) band for bare TMDC and TMDC/CrI<sub>3</sub> heterostructure (with WSe<sub>2</sub> and MoSe<sub>2</sub> as TMDC) in the presence or absence of the twist and SOC [63]. Notice that  $B_v$  changes sign in twisted cases.

### III. NUMERICAL RESULTS AND DISCUSSION

In this section, we mainly study the charge and thermal transport in the proposed F/S interface with the subgap energy regime. We concentrate on the Andreev differential conductance as well as the thermal conductance in the junction. Before presenting our numerical results, we should mention that the orbital gap  $\Delta$ , spin-orbit coupling  $\lambda_{c(v)}$  and the exchange interaction  $B_{c(v)}$  parameters for different TMDCs (like WSe<sub>2</sub> and MoSe<sub>2</sub>) are set to the values obtained in Ref. [63] [see Table. I].

Due to the vicinity to the 2D magnetic material, the magnetization direction of the TMDC is the same as in the I atoms of the monolayer CrI<sub>3</sub>, but opposite to the Cr atoms, resulting in a negative proximity exchange parameter. The absence or presence of the SOC term in the heterostructure calculations does not affect significant changes in the magnitude of the exchange parameters. However, twisting the CrI<sub>3</sub> layer relative to the TMDC changes the sign of the exchange field in the valence band and makes the valence band spin-splitting to be opposite in sign in the absence of SOC. The magnitude of the proximity exchanges  $B_v$  increases with twisting in WSe<sub>2</sub>-based heterostructure whereas it decreases in MoSe<sub>2</sub>-based heterostructure. Therefore, twisting can

remain an effective tool to modify the proximity exchange field. Since the parameters in the presence of the SOC in the heterostructure are barely various from those of the heterostructure without SOC, we set  $\Delta = 1.417(1.351)$  eV,  $\lambda_c = 13.81(-9.675)$  meV,  $\lambda_v = 240.99(94.43)$  meV,  $B_c = -1.648(-1.641)$  meV and  $B_v = 1.896(0.502)$  meV for twisted WSe<sub>2</sub> (MoSe<sub>2</sub>)/CrI<sub>3</sub> heterostructure with SOC.

The chemical potentials  $\mu_F$  and  $\mu_S$  are in units of eV. We set the zero-temperature superconducting order parameter  $\Delta_S = 1$  meV and scale the excitation energy,  $\varepsilon$ , in units of  $\Delta_S$  and the temperature  $T$  is in units of the critical temperature of the superconducting order parameter  $T_C$ .

#### A. Electrical conductance

To study electrical transport, we assume the F region is in contact with a biased reservoir, and that the S region is in contact with a reference reservoir. Applying a bias voltage  $V$  through the junction induces an electric current. In the Blonder-Tinkham-Klapwijk (BTK) formalism [22], the Andreev differential conductance at

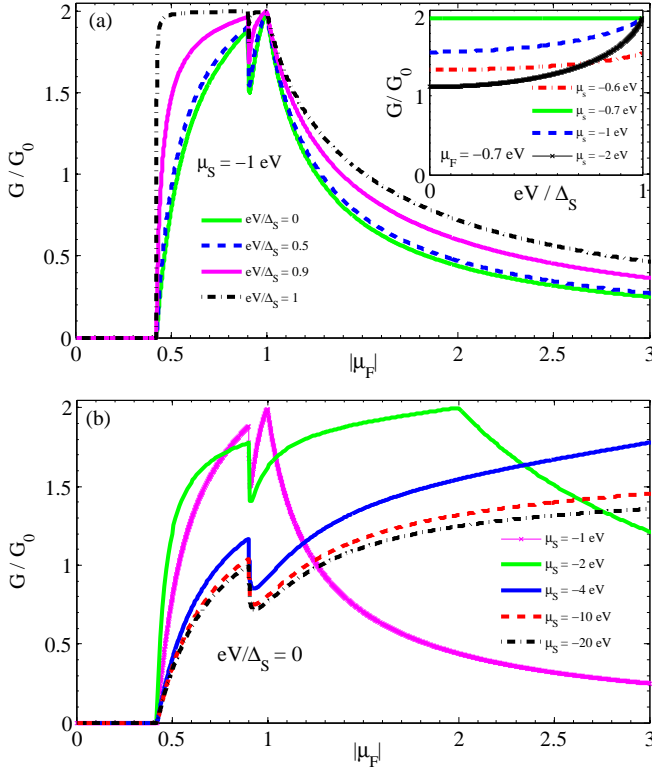


FIG. 1. (Color online) (a) The normalized Andreev differential conductance of the WSe<sub>2</sub>-based structure with *p*-doped F and S regions versus the magnitude of the chemical potential inside the F region,  $|\mu_F|$ , for different values of the subgap bias voltage  $eV/\Delta_S$ , when the chemical potential of the S region is set to  $\mu_S = -1$  eV. Inset of (a) presents the behavior of the Andreev conductance versus  $eV/\Delta_S$  for different values of  $\mu_S$ , when  $\mu_F = -0.7$  eV. (b) The behavior of the Andreev conductance versus  $|\mu_F|$  for different values of the chemical potential  $\mu_S$ , when  $eV/\Delta_S = 0$ . Note that there is no twist between the CrI<sub>3</sub> and the WSe<sub>2</sub> in the proposed structure.

zero temperature reads as

$$G(eV) = \sum_{s,\tau=\pm 1} G_0^{s,\tau}(eV) \int_0^{\theta_{s,\tau}^c} [1 - |r_{s,\tau}^e(\theta_{s,\tau}^e, eV)|^2 + |r_{\bar{s},\bar{\tau}}^h(\theta_{s,\tau}^e, eV)|^2] \cos \theta_{s,\tau}^e d\theta_{s,\tau}^e, \quad (20)$$

where  $G_0^{s,\tau}(eV) = e^2 W |\mathbf{k}_{s,\tau}^{e(h)}(eV)| / \pi h$  characterizes the spin-*s* valley- $\tau$  conductance of a TMDC/CrI<sub>3</sub> heterostructure of width *W* with perfect transmission. Here,  $\theta_{s,\tau}^c = \arcsin(|\mathbf{k}_{s,\tau}^h|/|\mathbf{k}_{s,\tau}^e|)$  is the critical angle of incidence above which the Andreev reflected waves become evanescent and do not contribute to any transport of charge. Herein, we have put  $\varepsilon = eV$  at zero temperature. Also, it is convenient to introduce the normalized conductance  $G/G_0$  with  $G_0 = \sum_{s,\tau=\pm 1} G_0^{s,\tau}$ .

Figure 1(a) shows the behavior of the normalized Andreev conductance  $G/G_0$  of *p*-doped WSe<sub>2</sub>-based structure in terms of the magnitude of the chemical potential

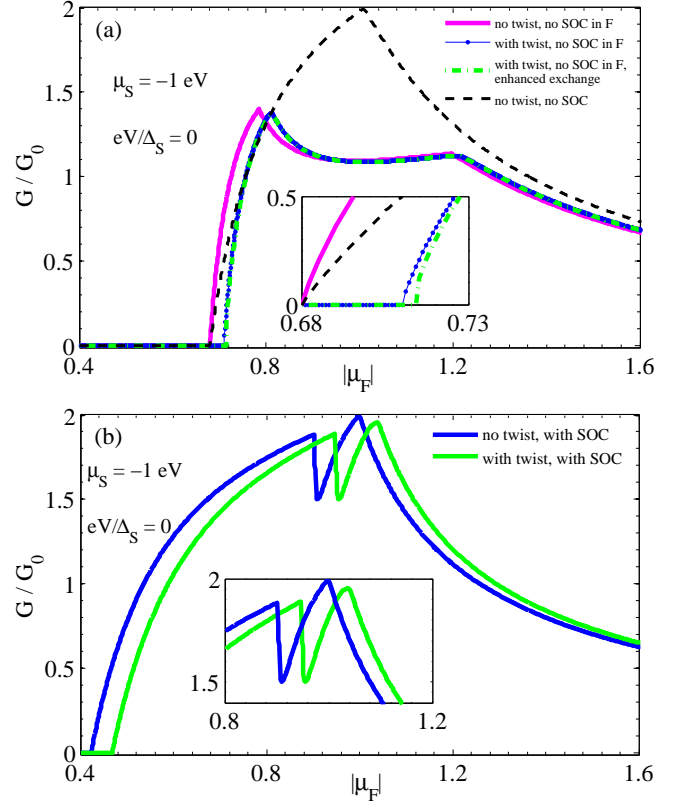


FIG. 2. (Color online) The zero-bias Andreev conductance as a function of the chemical potential  $|\mu_F|$  in the (a) absence and (b) presence of the spin-orbit coupling inside the F region, when  $\mu_S = -1$  eV. The twist angle between the CrI<sub>3</sub> and the WSe<sub>2</sub> is 30°. The enhancement of the proximity exchange interaction in the presence of the positive transverse electric field is about 4 meV.

inside the F region,  $|\mu_F|$ , when the chemical potential of the S region is set to  $\mu_S = -1$  eV. There is a wide gap in Andreev conductance owing to the orbital gap in the band structure of WSe<sub>2</sub>. Increasing the chemical potential of the F region leads to an enhancement of the zero-bias Andreev conductance and perfect AR with  $G/G_0 = 2$  occurs at  $|\mu_F| = |\mu_S|$ . Hereafter, it undergoes a decreasing behavior for  $|\mu_F| > |\mu_S|$ . Note that the presence of both the spin-orbit coupling and exchange coupling cause a cusp-like behavior at the edge of the spin- $\bar{s}$  valley- $\tau$  of the valence band with  $E_v^{\bar{s},\tau} = -\lambda_v + B_v - \Delta/2$ , so that for  $|\mu_F| < |E_v^{\bar{s}(s),\tau(\bar{\tau})}|$  the AR process is spin-polarized in each valley (with  $s\tau = 1$ ).

For subgap bias voltages, the probability of AR process and, therefore, the Andreev conductance increase by enhancing the  $eV/\Delta_S$  ratio and perfect AR occurs for a broad range of the chemical potential  $|\mu_F| \leq |\mu_S|$ , when  $eV/\Delta_S = 1$ . Inset of Fig. 1(a) demonstrates an enhancement of the Andreev conductance with respect to the  $eV/\Delta_S$  ratio for different values of the chemical potential  $\mu_S$ , such that perfect AR happens for all values of

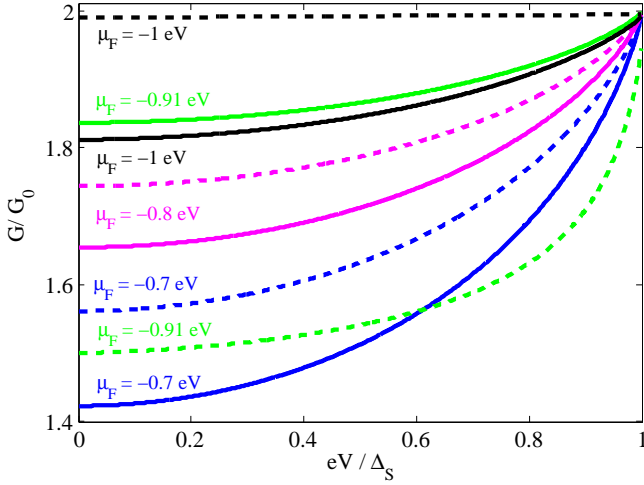


FIG. 3. (Color online) The bias voltage dependence of the Andreev conductance for the  $0^\circ$  (dashed lines) and  $30^\circ$  (solid lines) twist angles between the  $\text{CrI}_3$  and the  $\text{WSe}_2$  in  $\text{WSe}_2/\text{CrI}_3$  heterostructure, when  $\mu_F = -0.7, -0.8, -0.91$  and  $-1$  eV, and  $\mu_S = -1$  eV.

the subgap bias voltages when  $|\mu_S| = |\mu_F|$ . The Andreev conductance can be enhanced or reduced by increasing the chemical potential of the S region depending on the value of the bias voltage  $eV/\Delta_S$  ratio. Moreover, it is presented in Fig. 1(b) that the behavior of the Andreev conductance versus  $|\mu_F|$  is extremely sensitive to the value of the chemical potential inside the S region. The Andreev conductance has an increasing behavior with  $|\mu_F|$  for large values of  $\mu_S$ , while it experiences a decreasing behavior after a sharp peak at  $|\mu_F| = |\mu_S|$  for smaller values of  $\mu_S$ .

In the following, we evaluate the effect of the twist angle between the  $\text{CrI}_3$  and the  $\text{WSe}_2$  as well as the applied transverse electric field on the AR process and accordingly the Andreev conductance in the proposed structure. To obtain the effect of the twist angle, we turn off the SOC parameter [see Fig. 2(a)]. The absence of the SOC in the F region (magnetized gapped graphene/superconducting  $\text{WSe}_2$  structure) leads to various features of the Andreev conductance; it attenuates the Andreev conductance, prevents the perfect AR process (with  $G/G_0 = 2$ ), and removes the cusp-like behavior of the Andreev conductance. Most importantly, the twist angle-induced sign change of the proximity exchange in the valence band,  $B_v$ , leads to the suppression of the AR process and accordingly the Andreev conductance immediately after the wide gap in comparison to that of the untwisted structure. In particular, enhancement of the magnitude of the proximity exchange interaction by applying a positive gate electric field reduces the Andreev conductance and suppresses it in a broader range of the chemical potential  $\mu_F$  than that of the twisted one [see the inset of Fig. 2(a)]. In addition, it can be noted from Fig. 2(a) that the Andreev peak reap-

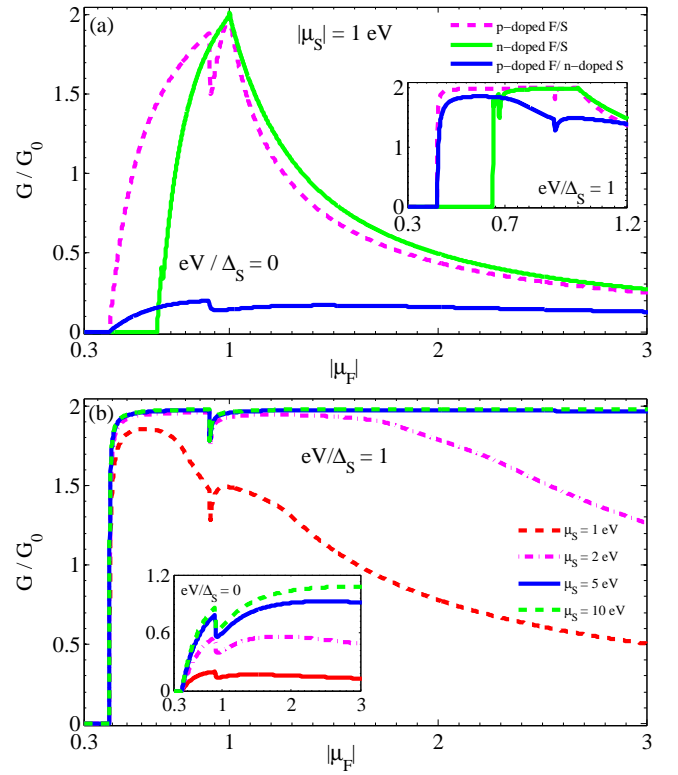


FIG. 4. (Color online) (a) The zero-bias Andreev conductance versus the magnitude of the chemical potential inside the F region for three different unstrained  $\text{WSe}_2$ -based structure with n- or p-type doped F and S regions. Inset of (a) shows the corresponding results for  $eV/\Delta_S = 1$ . (b) The behavior of the Andreev conductance for different values of the chemical potential  $\mu_S$  in F/S structure with n-doped S and p-doped F regions, when  $eV/\Delta_S = 0$  and 1.

pears at  $|\mu_F| = |\mu_S|$  if we switch off the SOC in both F and S regions (gapped graphene-based structure).

Turning on the SOC term in both regions ( $\text{WSe}_2$ -based structure) causes an Andreev peak at  $|\mu_F| = |\mu_S|$  as well as the cusp-like behavior of the Andreev conductance. Twisting the  $\text{CrI}_3$  with  $30^\circ$  relative to  $\text{WSe}_2$  stops the AR process for a wider range of  $\mu_F$  shifts the cusp to larger  $\mu_F$ , attenuates the conductance of the spin-valley polarized AR process, prevents perfect AR, and makes the Andreev conductance of the non-polarized AR process (after the cusp) to be increased or decreased depending on the value of  $\mu_F$  [see Fig. 2(b)]. Most importantly, as illustrated in Fig. 3, changes in the magnitude of the Andreev conductance in the presence of the twisting have its maximum value at zero bias  $eV/\Delta_S = 0$ , decreases with enhancing the subgap bias voltage and tends to zero for  $eV/\Delta_S = 1$ . However, in the case of  $\mu_F = -0.91$  eV (cusp position), twisting leads to an amplification of the Andreev conductance even at  $eV/\Delta_S = 1$ .

In addition, we present the chemical potential  $\mu_F$  dependence of the Andreev conductance for  $\text{WSe}_2$ -based

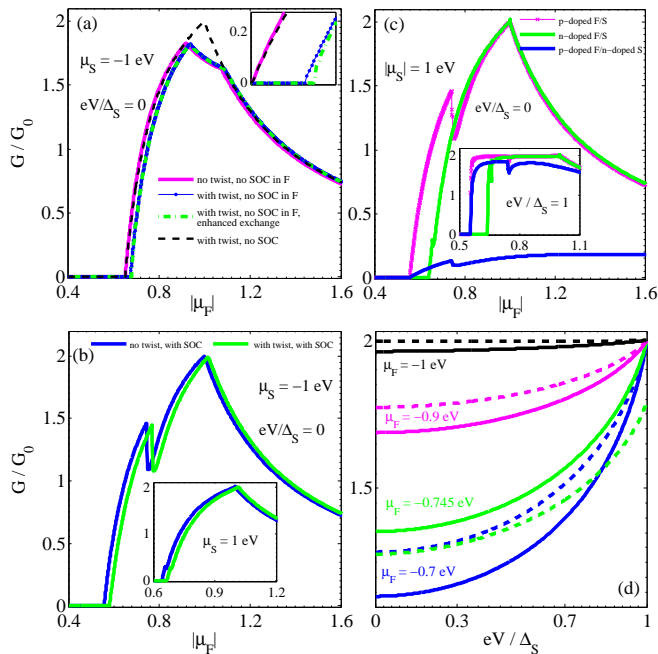


FIG. 5. (Color online) (a) The zero-bias Andreev conductance as a function of the chemical potential  $|\mu_F|$  in the (a) absence and (b) presence of the spin-orbit coupling inside the F region of p-doped MoSe<sub>2</sub>-based F/S structure, when  $\mu_S = -1$  eV. Enhancement of the magnitude of the proximity exchange interaction in the presence of the positive transverse electric field is about 4 meV. (c) The zero-bias Andreev conductance versus  $|\mu_F|$  for three different unstrained MoSe<sub>2</sub>-based structure with n- or p-type doped F and S regions. Inset shows the corresponding results for  $eV/\Delta_S = 1$ . (d) The bias voltage dependence of the Andreev conductance for different values of the chemical potential  $\mu_F$  in untwisted (dashed lines) and twisted (solid lines) p-doped MoSe<sub>2</sub>-based structure, when  $\mu_S = -1$  eV.

F/S structures with various types of doping for the F and S regions in Fig. 4(a), when  $|\mu_S| = 1$  eV and  $eV/\Delta_S = 0$  and 1. In the case of n-type doping, a wide zero conductance gap, spin-valley polarized AR process for a small range of  $|\mu_F|$  and enhanced zero-bias Andreev conductance for  $|\mu_F| > |\mu_S|$  are seen. Significantly, AR process with unit efficiency occurs for a smaller range of  $|\mu_F|$  in contrast to that of the p-type structure when  $eV/\Delta_S = 1$ . On the other hand, a strong reduction of the zero-bias Andreev conductance, as well as different qualitative behavior with non-perfect AR for  $eV/\Delta_S = 1$ , can be seen in the corresponding structure with n-doped S and p-doped F regions. Interestingly, we find that the amplification of the Andreev conductance and accordingly the AR process with unit efficiency (almost for all values of  $\mu_F$ ) can be achieved for p-doped F/n-doped S junction by enhancing the magnitude of the chemical potential inside the S region [see Fig. 4(b)].

We evaluate the behavior of the Andreev conductance of the MoSe<sub>2</sub>-based F/S structure in Fig. 5. In com-

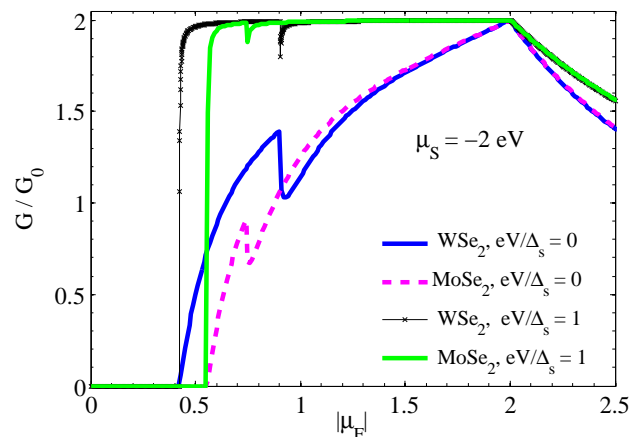


FIG. 6. (Color online) Andreev conductance as a function of  $|\mu_F|$  for p-doped WSe<sub>2</sub>- and MoSe<sub>2</sub>-based F/S structures with  $\mu_S = -2$  eV, when  $eV/\Delta_S = 0$  and 1.

parison to the WSe<sub>2</sub>-based structure, a slight reduction of the Andreev conductance in the absence of the SOC term in the F region is obvious from Fig. 5(a). A cusp-like behavior is present away from the Andreev peak, at a minor value of the chemical potential inside the F region [see Fig. 5(b)]. Astonishingly, a twist angle induced amplification of the Andreev conductance increases with the subgap bias voltage for the chemical potential  $\mu_F = -0.745$  eV, being at the cusp position, while it decreases with  $eV/\Delta_S$  for WSe<sub>2</sub>-based structure [see Fig. 5(d)]. In addition, it can be perceived from Fig. 5(c) that p-doped F/S junction has higher spin-valley polarized Andreev conductance in comparison to the n-type one at zero bias voltage and perfect electron-hole conversion occurs for a wide range of  $\mu_F$ , when  $eV/\Delta_S = 1$ .

Furthermore, we compare the results with those of the WSe<sub>2</sub>-based structure with p-doped F and S regions in Fig. 6. It turns out that the suppression of the AR for a broad range of the chemical potential  $\mu_F$  as well as reduction of the Andreev conductance for other values of  $\mu_F$  occur in the MoSe<sub>2</sub>-based structure. We note that the spin-splitting of the valence band in the WSe<sub>2</sub>-based structure is considerably larger than that of the MoSe<sub>2</sub>, because of the strong spin-orbit coupling.

## B. Thermal conductance

We now turn to investigate the thermal transport properties of the proposed F/S structure. Applying a temperature gradient  $\Delta T$  through the junction, we can calculate the thermal conductance  $\kappa = \lim_{\Delta T \rightarrow 0} J_{th}/\Delta T$ , with  $J_{th}$  the heat current density, by incorporating the low-energy



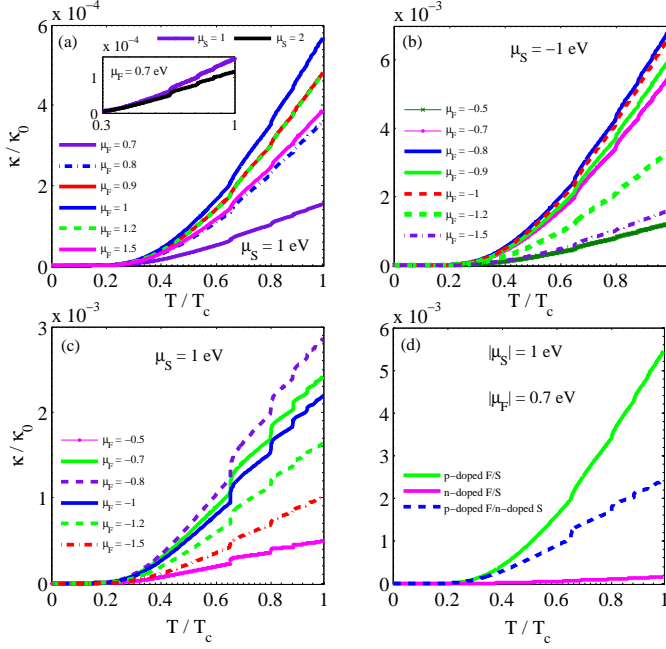


FIG. 7. (Color online) The behavior of the normalized thermal conductance in terms of the temperature  $T/T_C$  for different values of the chemical potential  $\mu_F$  in untwisted WSe<sub>2</sub>-based (a) n-doped F/S (b) p-doped F/S (c) p-doped F/n-doped S junction, when  $|\mu_S| = 1$  eV. Inset of (a) shows the behavior of the thermal conductance vs  $T/T_C$  for two values of  $\mu_S$ , when  $\mu_F = 0.7$  eV. The comparison of the thermal conductance for different types of doping in F/S structure are illustrated in (d), when  $|\mu_F| = 0.7$  eV and  $|\mu_S| = 1$  eV.

excitations as follows [66, 67]

$$\kappa = \frac{k_B W}{4\pi^2 \hbar} \sum_{s,\tau=\pm 1} \int_0^\infty \int_0^{\pi/2} d\varepsilon d\theta_{s,\tau}^e \frac{\varepsilon^2 |\mathbf{k}_{s,\tau}^e(\varepsilon)| \cos \theta_{s,\tau}^e}{(k_B T)^2 \cosh^2(\frac{\varepsilon}{2k_B T})} \times [1 - |r_{s,\tau}^e(\theta_{s,\tau}^e, \varepsilon)|^2 - \text{Re}(\frac{\cos \theta_{s,\tau}^h}{\cos \theta_{s,\tau}^e} |r_{\bar{s},\bar{\tau}}^h(\theta_{s,\tau}^e, \varepsilon)|^2)], \quad (21)$$

where  $T$  is the thermal equilibrium temperature and we replace the zero-temperature superconducting order parameter  $\Delta_S$  in Eq. (8) with the temperature-dependent one,  $\Delta_S(T) = 1.76 k_B T_C \tanh(1.74 \sqrt{T_C/T} - 1)$ . Also, we set  $k_B = 1$ .

Figures 7(a)-7(c) illustrate the behavior of the normalized thermal conductance  $\kappa/\kappa_0$  (with  $\kappa_0 = k_B W \sum_{s,\tau=\pm 1} \int_0^\infty d\varepsilon |\mathbf{k}_{s,\tau}^e(\varepsilon)|/4\pi^2 \hbar$ ) in terms of the temperature  $T/T_C$  respectively for n-doped F/S, p-doped F/S, and p-doped F/n-doped S junctions with various values of the chemical potential  $\mu_F$ , when  $|\mu_S| = 1$  eV. It is noted that the thermal conductance, in contrast to the Andreev conductance, is suppressed by AR at low temperatures. The physical reason is Cooper pairs carry a finite charge ( $2e$ ), but zero heat across the junction. For the thermal conductance to be finite, the temperature

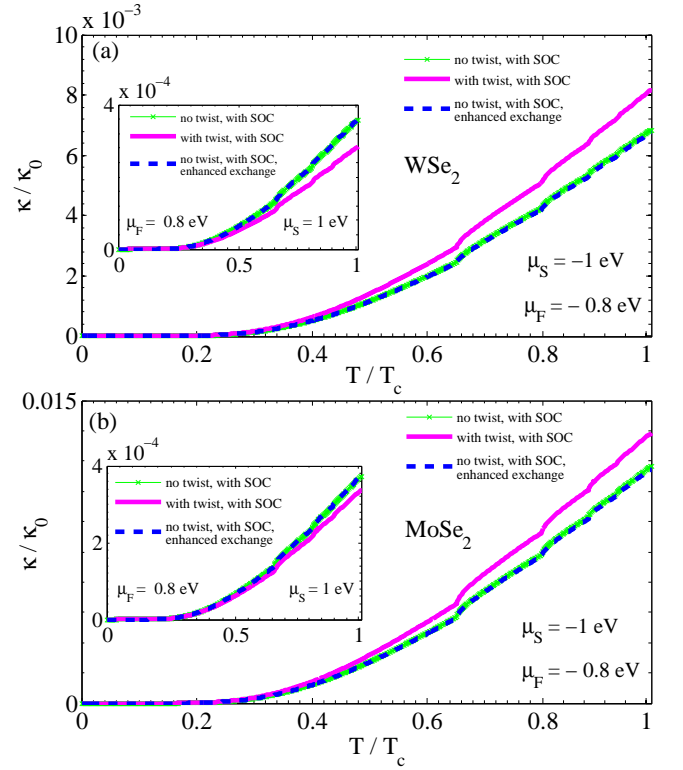


FIG. 8. (Color online) The effect of the twist angle between the CrI<sub>3</sub> and the TMDC layer and the enhanced exchange coupling (of about 4 meV by positive gate electric field) on the thermal conductance of untwisted (a) WSe<sub>2</sub>- and (b) MoSe<sub>2</sub>-based p-doped F/S structures with  $\mu_F = -0.8$  eV and  $\mu_S = -1$  eV. Insets show the corresponding results for n-doped F/S junctions.

must be so high that electron-like and hole-like quasiparticles can be transmitted into the S region. Therefore, the more significant transmission of quasiparticles at higher temperatures results in an increasing behavior of the thermal conductance with increasing the temperature. It turns out that increasing the magnitude of the chemical potential inside the F region leads to the enhancement of the thermal conductance of n-doped F/S (p-doped F/n-doped S) structure for  $\mu_F \leq \mu_S$  ( $|\mu_F| \leq 0.8 \mu_S$ ) and reduction of it for  $\mu_F > \mu_S$  ( $|\mu_F| > 0.8 \mu_S$ ) [see Figs. 7(a) and 7(c)]. In contrast, varying the type of doping in F and S regions from n-type to p-type causes the thermal conductance of p-doped F/S structure to be increased or decreased with enhancing the chemical potential  $|\mu_F|$  [see Figs. 7(b)]. Moreover, it is singled out from the inset of Fig. 7(a) that enhancing the chemical potential  $\mu_S$  tends to reduce the thermal conductance. Comparing the results of thermal conductance for F/S structures with various types of doping for F and S regions show that, in contrast to the Andreev conductance, n-doped F/S structure has a very small thermal conductance and importantly p-doped structure possesses a significant en-

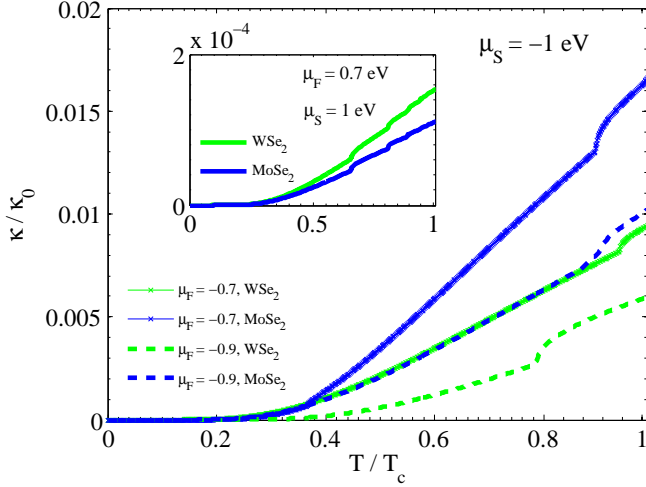


FIG. 9. (Color online) Thermal conductance versus  $T/T_C$  for two values of  $\mu_F$  in WSe<sub>2</sub>- and MoSe<sub>2</sub>-based p-doped F/S structures. Inset shows the corresponding results for n-doped F/S junctions.

enhancement for the thermal conductance in comparison to that of the p-doped F/n-doped S structure. Similar results are obtained for the corresponding MoSe<sub>2</sub>-based F/S junctions with n-type S region [see appendix A]. The difference is that enhancing the value of the chemical potential inside the S region tends to increase the thermal conductance [see the inset of Fig. 11(a)]. Also, the behavior of the thermal conductance of the p-doped F/S structure is similar to that of the p-doped F/n-doped S structure.

In addition, we evaluate the effect of the twist angle as well as the gate electric field on the thermal conductance of WSe<sub>2</sub>- and MoSe<sub>2</sub>-based F/S junctions, respectively, in Figs. 8(a) and 8(b). It is worth noting that twisting tends to enhance the thermal conductance of both WSe<sub>2</sub>- and MoSe<sub>2</sub>-based structures with p-type doping, whereas it reduces the thermal conductance of the corresponding structures with n-type doping. The magnitude of the proximity exchange coupling increases by applying a positive gate electric field and produces an extremely small reduction in the thermal conductance of both WSe<sub>2</sub>- and MoSe<sub>2</sub>-based structures with p-type doping. We have found that the thermal conductance in the absence of the SOC term in the F or (and) S region, magnetized gapped graphene/ WSe<sub>2</sub> (gapped graphene-based) structure, is significantly larger than that of the WSe<sub>2</sub>-based structure [see appendix B]. Most importantly, it is illustrated in Fig. 9 that replacing WSe<sub>2</sub> layer with MoSe<sub>2</sub> results in an enhancement of the thermal conductance of p-doped structure, but the reduction of the thermal conductance in corresponding structure with n-type doping.

Ultimately, we present the chemical potential dependence of the thermal conductance of WSe<sub>2</sub>-based F/S structures with various types of doping for the F and S

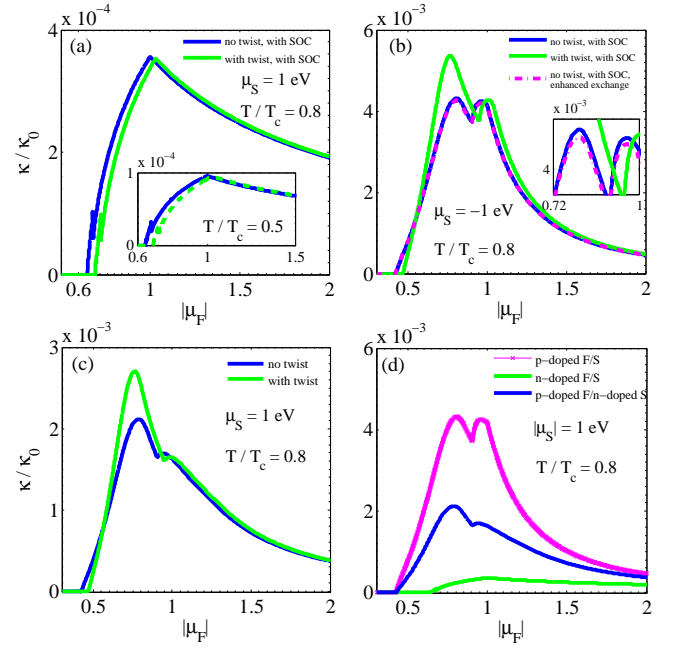


FIG. 10. (Color online) The chemical potential dependence of the thermal conductance in the absence and presence of the twist angle between the CrI<sub>3</sub> and the WSe<sub>2</sub> layer in (a) n-doped F/S (b) p-doped F/S and (c) p-doped F/n-doped S structures with  $|\mu_S| = 1$  eV, when  $T/T_C = 0.8$ . (d) Comparing the thermal conductance of F/S structures with various types of doping. Insets of (a) and (b) respectively present the chemical potential dependence of the thermal conductance for  $T/T_C = 0.5$  and the zoomed-in view of the  $\kappa/\kappa_0$  ratio in the range  $0.72 \leq |\mu_F| \leq 1$ .

regions in Fig. 10, when  $|\mu_S| = 1$  eV. In the case of n-doped F/S structure, it is perceived that the thermal conductance experiences a cusp-like behavior after a gap for  $\mu_F < -B_c - \lambda_c + \Delta/2$ , increases with  $\mu_F$  for  $\mu_F < \mu_S$  and after reaching a maximum at  $\mu_F = \mu_S$  it decreases for  $\mu_F > \mu_S$  [see Fig. 10(a)]. Twisting the CrI<sub>3</sub> with respect to the WSe<sub>2</sub> layer suppresses the thermal conductance for a wider range of  $\mu_F$ . Increasing the chemical potential of the F region makes the thermal conductance decrease relative to the untwisted one for  $\mu_F < \mu_S$ . The twist-angle induced changes in the magnitude of the thermal conductance decrease with increasing  $\mu_F$  and tend to zero at low  $T/T_C$  ratio, when  $\mu_F \rightarrow \mu_S$  [see the inset of Fig. 10(a)]. Nevertheless, increasing the  $T/T_C$  ratio can lead to an enhancement of the thermal conductance in the presence of the twisting for  $\mu_F > \mu_S$ . Figures 10(b) and 10(c) indicate that twisting causes the thermal conductance of F/S structures with p-doped F region to be decreased or increased with respect to that of the untwisted structures for the chemical potentials  $|\mu_F| < |\mu_S|$ , however, it leads to small enhancement of  $\kappa$  for  $|\mu_F| \geq |\mu_S|$ . Moreover, it is noted from the inset of Fig. 10(b) that the gate electric field-induced enhancement of the proximity exchange coupling results in a slight reduction of the thermal con-

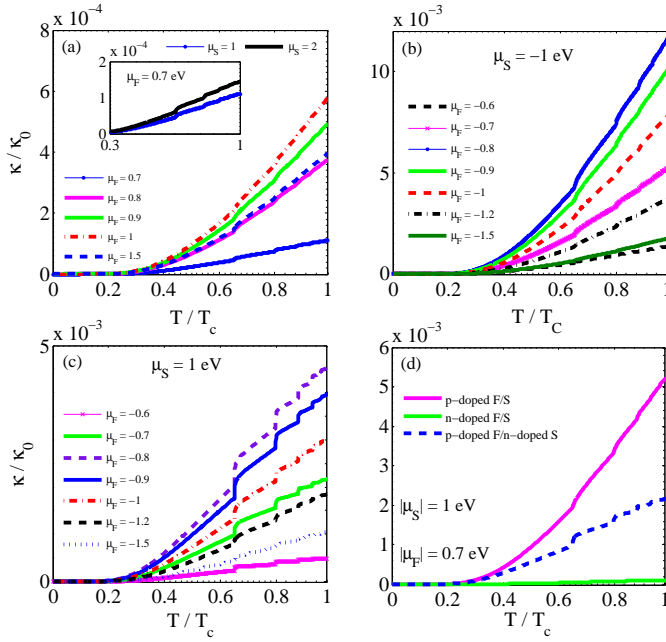


FIG. 11. (Color online) Thermal conductance in terms of the temperature  $T/T_C$  for different values of the chemical potential  $\mu_F$  in untwisted MoSe<sub>2</sub>-based (a) n-doped F/S (b) p-doped F/S (c) p-doped F/n-doped S junction, when  $|\mu_S| = 1$  eV. (d) Comparison of the thermal conductance for F/S structures with different types of doping, when  $|\mu_F| = 0.7$  eV and  $|\mu_S| = 1$  eV.

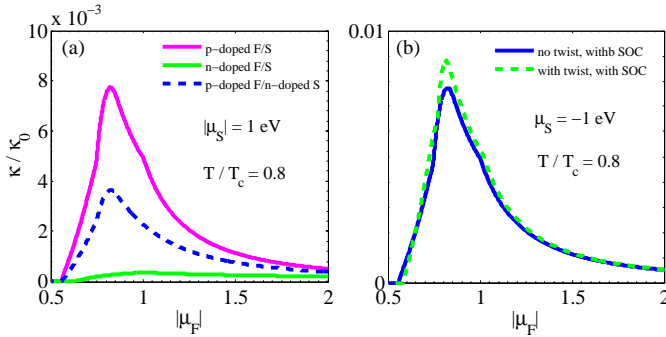


FIG. 12. (Color online) The chemical potential dependence of the thermal conductance of MoSe<sub>2</sub>-based F/S structures (a) with various types of doping for F and S regions and (b) in the absence and presence of twisting for p-type doping, when  $|\mu_S| = 1$  eV and  $T/T_C = 0.8$ .

ductance. Comparing the results of thermal conductance for various types of doping in F/S structures confirm that the high thermal conductance belongs to p-doped structure and the F/S structure with n-type doping has low thermal conductance [see Fig. 10(d)].

#### IV. CONCLUSION

In summary, we have studied the electrical and thermal transport characteristics of a twisted TMDC/CrI<sub>3</sub> heterostructure (as ferromagnetic region) connected to a superconducting TMDC layer, within the scattering formalism. It is revealed that the spin-valley polarized Andreev reflection (AR) can be effectively modulated by tuning the charge doping, twisting the monolayer CrI<sub>3</sub> with respect to the TMDC layer, and applying a gate electric field. The perfect AR is visible for subgap bias voltages  $eV < \Delta_S$  when the chemical potential of the ferromagnetic region  $\mu_F$ , in p- or n-type doped structure, is equal to that of the superconducting region  $\mu_S$ , and over a wide range of  $\mu_F$  ( $|\mu_F| \leq |\mu_S|$ ) when  $eV = \Delta_S$ . The twist angle between the CrI<sub>3</sub> and the TMDC (with WSe<sub>2</sub> and MoSe<sub>2</sub> as TMDC) leads to the suppression or reduction of the spin-valley polarized Andreev conductance and the enhancement of the non-spin-valley polarized Andreev conductance, depending on the chemical potential  $\mu_F$ . Changes in the magnitude of the Andreev conductance by twisting are reduced to increasing the subgap bias voltage and could be vanished at  $eV = \Delta_S$  in WSe<sub>2</sub>-based structure. However, it can be enhanced by increasing the bias voltage at the defined chemical potential of the ferromagnetic region in the MoSe<sub>2</sub>-based structure.

We have further analyzed the effect of twisting on the thermal conductance and demonstrated that an amplification of the thermal conductance can occur for  $|\mu_F| < |\mu_S|$  in the proposed structure with p-type doping, whereas it will be reduced in n-doped structure. Furthermore, enhancing the proximity exchange by applying a positive gate electric field to the TMDC/CrI<sub>3</sub> heterostructure slightly reduces the thermal conductance of p-type doping as well as the probability of AR process, and accordingly the Andreev conductance and suppresses it for small values of  $\mu_F$ . Moreover, we have shown that Andreev and thermal conductance can be changed significantly by tuning the type of charge doping in ferromagnetic and superconducting regions. The proposed structure displays high Andreev and thermal conductance in the case of p-type doping. We have further found that the low charge conductance of the p-doped ferromagnetic/n-doped superconducting junction can be increased remarkably by increasing the chemical potential of the superconducting region such that perfect AR can occur for almost all values of  $\mu_F$  when  $eV = \Delta_S$ .

In addition, our results show that replacing WSe<sub>2</sub> with MoSe<sub>2</sub> tends to attenuate the Andreev conductance as well as the amplification of the thermal conductance in p-doped F/S structure, and reduction of the thermal conductance in n-type doped structure. Moreover, turning off the spin-orbit interaction in the structure by using gapped graphene in one or both ferromagnetic and superconducting regions causes significant changes in the electrical and thermal conductance of the proposed structure. Our theoretical funding can be explored by current

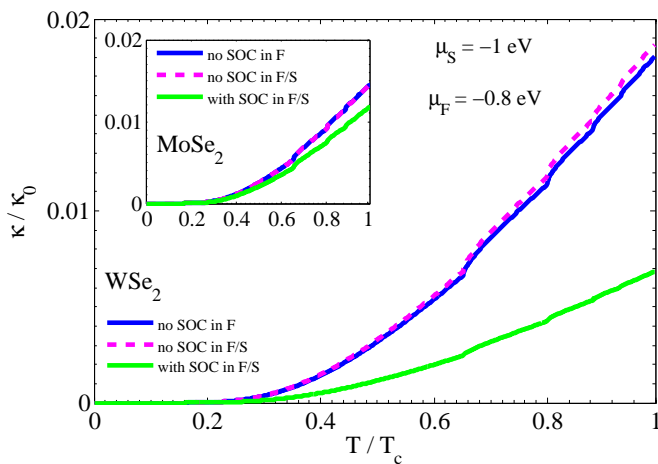


FIG. 13. (Color online) Thermal conductance in terms of the temperature  $T/T_C$  in the absence and presence of spin-orbit coupling in untwisted WSe<sub>2</sub>-based p-doped F/S junction, when  $\mu_F = -0.8$  eV and  $\mu_S = -1$  eV. Inset shows the corresponding results for MoSe<sub>2</sub>-based F/S junction.

experiments.

## ACKNOWLEDGMENTS

This work is supported by Iran Science Elites Federation.

### Appendix A: Thermal conductance of MoSe<sub>2</sub>-based F/S structure with various types of charge doping for F and S regions

The behavior of the normalized thermal conductance  $\kappa/\kappa_0$  in terms of the temperature  $T/T_C$  are illustrated in Figs. 11(a)-11(c) respectively for the n-doped F/S, p-doped F/S, and p-doped F/n-doped S junctions with various values of the chemical potential  $\mu_F$ , when  $|\mu_S| = 1$  eV. The thermal conductance has an increasing behav-

ior with the temperature. Similar to the WSe<sub>2</sub>-based structures, the thermal conductance increases with enhancing the magnitude of the chemical potential inside the F region of n-doped F/S (p-doped F/n-doped S) structure for  $\mu_F \leq \mu_S$  ( $|\mu_F| \leq 0.8 |\mu_S|$ ) and decreases for  $\mu_F > \mu_S$  ( $|\mu_F| > 0.8 |\mu_S|$ ). However, in contrast to WSe<sub>2</sub>-based structure, the thermal conductance of p-type doped structure increases with enhancing  $|\mu_F|$  for  $|\mu_F| \leq 0.8 |\mu_S|$  and decreases for  $|\mu_F| > 0.8 |\mu_S|$ . Besides, the thermal conductance can be increased by enhancing the chemical potential of the S region [see the inset of Fig.11(a)]. We further demonstrate the amplification of the thermal conductance in F/S structures with p-doped F region in comparison to that of the n-type doping [see Fig. 11(d)].

In addition, it is presented in Fig. 12 that the peak structure of the thermal conductance in terms of  $|\mu_F|$  in MoSe<sub>2</sub>-based F/S structures are different from those of the corresponding WSe<sub>2</sub>-based structures. Also, the high thermal conductance of p-doped structure in comparison to that of the n-doped structure is obvious from Fig. 12(a). It can be seen from Fig. 12(b) that twisting tends to the amplification of the thermal conductance in a wide range of  $\mu_F$ . However, we have found (not shown) that the enhancement of the proximity exchange by the positive gate electric field leads to the small reduction of the thermal conductance around the peak.

### Appendix B: The effect of spin-orbit interaction on the thermal conductance of WSe<sub>2</sub>- and MoSe<sub>2</sub>-based F/S junctions

Figure 13 shows that the thermal conductance in the absence of the SOC term in the F region (magnetized gapped graphene/ superconducting WSe<sub>2</sub> structure) as well as the F/S structure without SOC term (gapped graphene-based structure) are significantly larger than that of the WSe<sub>2</sub>-based structure. Inset of Fig. 13 presents less enhancement of the thermal conductance in the corresponding structures based on MoSe<sub>2</sub>.

- 
- [1] R. Yan, G. Khalsa, S. Vishwanath, Y. Han, J. Wright, S. Rouvimov, D. S. Katzer, N. Nepal, B. P. Downey, D. A. Muller, H. G. Xing, D. J. Meyer, and D. Jena, *Nature (London)* **555**, 183 (2018).
  - [2] V. V. Ryazanov, V. A. Oboznov, A. Y. Rusanov, A. V. Veretennikov, A. A. Golubov, and J. Aarts, *Phys. Rev. Lett.* **86**, 2427 (2001).
  - [3] J. W. A. Robinson, J. D. S. Witt, and M. G. Blamire, *Science* **329**, 59 (2010).
  - [4] M. Eschrig, J. Kopu, J. C. Cuevas, and G. Schon, *Phys. Rev. Lett.* **90**, 137003 (2003).
  - [5] R. M. Lutchyn, J. D. Sau, and S. Das Sarma, *Phys. Rev. Lett.* **105**, 077001 (2010).
  - [6] B. Baek, W. H. Rippard, S. P. Benz, S. E. Russek, and P. D. Dresselhaus, *Nat. Commun.* **5**, 3888 (2014).
  - [7] M. Eschrig, *Rep. Prog. Phys.* **78**, 104501 (2015).
  - [8] I. Žutić, J. Fabian, and S. Das Sarma, *Rev. Mod. Phys.* **76**, 323 (2004).
  - [9] Y. Nakamura, C. D. Chen and J. S. Tsai, *Phys. Rev. Lett.* **79**, 2328 (1997).
  - [10] S. Han, Y. Yu, X. Chu, S. Chu and Z. Wang, *Science* **293** 1457, (2001).
  - [11] D. Vion, A. Aassime, A. Cottet, O. Joyez, H. Pothier, C. Urbina, D. Esteve and M. H. Devoret, *Science* **296**, 886 (2002).
  - [12] J. M. Martinis, S. Nam, J. Aumentado and C. Urbina, *Phys. Rev. Lett.* **89**, 117901 (2002).



- [13] F. Arute *et al.*, Nature (London) **574**, 505 (2019).
- [14] S. K. Upadhyay, A. Palanisami, R. N. Louie, and R. A. Buhrman, Phys. Rev. Lett. **81**, 3247 (1998).
- [15] R. J. Soulen, J. M. Byers, M. S. Osofsky, B. Nadgorny, T. Ambrose, S. F. Cheng, P. R. Broussard, C. T. Tanaka, J. Nowak, J. S. Moodera, A. Barry, and J. M. D. Coey, Science **282**, 85 (1998).
- [16] I. I. Mazin, Phys. Rev. Lett. **83**, 1427 (1999).
- [17] R. Meservey and P. Tedrow, Phys. Rep. **238**, 173 (1994).
- [18] M. Bode, Rep. Prog. Phys. **66**, 523 (2003).
- [19] G. Annunziata, M. Cuoco, P. Gentile, A. Romano, and C. Noce, Phys. Rev. B **83**, 094507 (2011).
- [20] D. Daghero, M. Tortello, G. A. Ummarino, and R. S. Gonnelli, Rep. Prog. Phys. **74**, 124509 (2011).
- [21] A. F. Andreev, Sov. Phys. JETP **19**, 1228 (1964).
- [22] G. E. Blonder, M. Tinkham, and T. M. Klapwijk, Phys. Rev. B **25**, 4515 (1982).
- [23] R. A. Riedel and P. F. Bagwell, Phys. Rev. B **48**, 15198 (1993).
- [24] S. Lee, V. Stanev, X. Zhang, D. Stasak, J. Flowers, J. S. Higgins, S. Dai, T. Blum, X. Pan, V. M. Yakovenko, J. Paglione, R. L. Greene, V. Galitski, and I. Takeuchi, Nature (London) **570**, 344 (2019).
- [25] M. J. M. de Jong and C. W. J. Beenakker, Phys. Rev. Lett. **74**, 1657 (1995).
- [26] C. W. J. Beenakker, Phys. Rev. Lett. **97**, 067007 (2006).
- [27] L. Majidi and R. Asgari, Phys. Rev. B **93**, 195404 (2016).
- [28] L. Majidi, M. Zare and R. Asgari, Physica C **549**, 77-80 (2018).
- [29] M. Zareyan, H. Mohammadpour, and A. G. Moghaddam, Phys. Rev. B **78**, 193406 (2008).
- [30] L. Majidi and M. Zareyan, Phys. Rev. B **86**, 075443 (2012).
- [31] L. Majidi and M. Zareyan, J. Comput. Electron. **12**, 134 (2013).
- [32] D. K. Efetov, L. Wang, C. Handschin, K. B. Efetov, J. Shuang, R. Cava, T. Taniguchi, K. Watanabe, J. Hone, C. R. Dean and P. Kim, Nat. Phys. **12**, 328-332 (2016).
- [33] J. Cayssol, Phys. Rev. Lett. **100**, 147001 (2008).
- [34] J. Linder, M. Zareyan, and A. Sudbø, Phys. Rev. B **80**, 014513 (2009).
- [35] J. Wang and S. Liu, Phys. Rev. B **85**, 035402 (2012).
- [36] J. Linder and T. Yokoyama, Phys. Rev. B **89**, 020504(R) (2014).
- [37] L. Majidi and R. Asgari, Phys. Rev. B **90**, 165440 (2014).
- [38] P. Pandey, R. Danneau, and D. Beckmann, Phys. Rev. Lett. **126**, 147701 (2021).
- [39] L. Majidi and R. Asgari, New J. Phys. **22**, 123033 (2020).
- [40] A. K. Geim and I. V. Grigorieva, Nature (London) **499**, 419-425 (2013).
- [41] K. S. Novoselov, A. Mishchenko, A. Carvalho, and A. H. C. Neto, Science **353**, 9439 (2016).
- [42] J. F. Sierra, J. Fabian, R. K. Kawakami, S. Roche and S. O. Valenzuela, Nat. Nanotechnol. **16**, 856-868 (2021).
- [43] K. F. Mak, Ch. Lee, J. Hone, J. Shan, and T. F. Heinz, Phys. Rev. Lett. **105**, 136805 (2010).
- [44] A. Splendiani, L. Sun, Y. Zhang, T. Li, J. Kim, Ch.-Y. Chim, G. Galli, and F. Wang, Nano Lett. **10**, 1271 (2010).
- [45] T. Korn, S. Heydrich, M. Hirmer, J. Schmutzler, and C. Schüller, Appl. Phys. Lett. **99**, 102109 (2011).
- [46] D. Xiao, G.-B. Liu, W. Feng, X. Xu, and W. Yao, Phys. Rev. Lett. **108**, 196802 (2012).
- [47] S. I. Vishkayi, Z. Torbatian, A. R. Qaiumzadeh and R. Asgari, Phys. Rev. Materials **4**, 094004 (2020).
- [48] B. Huang, G. Clark, E. Navarro-Moratalla, D. R. Klein, R. Cheng, K. L. Seyler, D. Zhong, E. Schmidgall, M. A. McGuire, D. H. Cobden, W. Yao, D. Xiao, P. Jarillo-Herrero, and X. Xu, Nature (London) **546**, 270 (2017).
- [49] P. Jiang, C. Wang, D. Chen, Z. Zhong, Z. Yuan, Z.-Y. Lu, and W. Ji, Phys. Rev. B **99**, 144401 (2019).
- [50] S. Jiang, J. Shan, and K. F. Mak, Nat. Mater. **17**, 406 (2018).
- [51] T. Song, X. Cai, M. W.-Y. Tu, X. Zhang, B. Huang, N. P. Wilson, K. L. Seyler, L. Zhu, T. Taniguchi, K. Watanabe, M. A. McGuire, D. H. Cobden, D. Xiao, W. Yao, and X. Xu, Science **360**, 1214 (2018).
- [52] B. Radisavljevic, A. Radenovic, J. Brivio, V. Giacometti, and A. Kis, Nat. Nanotechnol. **6**, 147 (2011).
- [53] M. Fontana, T. Deppe, A. K. Boyd, M. Rinzan, A. Y. Liu, M. Paranjape, and P. Barbara, Sci. Rep. **3**, 1634 (2013); M. R. Laskar *et al.*, Appl. Phys. Lett. **104**, 092104 (2014).
- [54] T. K. Gupta, Phys. Rev. B **43**, 5276 (1991).
- [55] K. Taniguchi, A. Matsumoto, H. Shimotani, and H. Takagi, Appl. Phys. Lett. **101**, 042603 (2012).
- [56] J. T. Ye, Y. J. Zhang, R. Akashi, M. S. Bahramy, R. Arita, and Y. Iwasa, Science **338**, 1193 (2012).
- [57] R. Roldán, E. Cappelluti, and F. Guinea, Phys. Rev. B **88**, 054515 (2013); Y. Ge and A. Y. Liu, *ibid.* **87**, 241408 (2013).
- [58] A. L. Sharpe, E. J. Fox, A. W. Barnard, J. Finney, K. Watanabe, T. Taniguchi, M. A. Kastner, and D. Goldhaber-Gordon, Science **365**, 605-608 (2019).
- [59] Y. Cao, V. Fatemi, Sh. Fang, K. Watanabe, T. Taniguchi, E. Kaxiras and P. Jarillo-Herrero, Nature (London) **556**, 43-50 (2018).
- [60] L. Balents, C. R. Dean, D. K. Efetov and A. F. Young, Nat. Phys. **16**, 725-733 (2020).
- [61] T. Naimier, K. Zollner, M. Gmitra, and J. Fabian, Phys. Rev. B **104**, 195156 (2021).
- [62] K. Zollner, and J. Fabian, arXiv:2108.03984v1.
- [63] K. Zollner, P. E. Faria Junior, and J. Fabian, Phys. Rev. B **100**, 085128 (2019).
- [64] L. Majidi, H. Rostami, and R. Asgari, Phys. Rev. B **89**, 045413 (2014).
- [65] L. Majidi, M. Zare, and R. Asgari, Solid State Commun. **199** 52 (2014).
- [66] A. Bardas and D. Averin, Phys. Rev. B **52**, 12873 (1995).
- [67] T. Yokoyama, J. Linder, and A. Sudbø, Phys. Rev. B **77**, 132503 (2008).